

MASt3R-Fusion: Integrating Feed-Forward Visual Model with IMU, GNSS for High-Functionality SLAM

Yuxuan Zhou, Xingxing Li*, Shengyu Li, Zuoohao Yan, Chunxi Xia, Shaoquan Feng

Abstract—Visual SLAM is a cornerstone technique in robotics, autonomous driving and extended reality (XR), yet classical systems often struggle with low-texture environments, scale ambiguity, and degraded performance under challenging visual conditions. Recent advancements in feed-forward neural network-based pointmap regression have demonstrated the potential to recover high-fidelity 3D scene geometry directly from images, leveraging learned spatial priors to overcome limitations of traditional multi-view geometry methods. However, the widely validated advantages of probabilistic multi-sensor information fusion are often discarded in these pipelines. In this work, we propose *MASt3R-Fusion*, a multi-sensor-assisted visual SLAM framework that tightly integrates feed-forward pointmap regression with complementary sensor information, including inertial measurements and GNSS data. The system introduces Sim(3)-based visual alignment constraints (in the Hessian form) into a universal metric-scale SE(3) factor graph for effective information fusion. A hierarchical factor graph design is developed, which allows both real-time sliding-window optimization and global optimization with aggressive loop closures, enabling real-time pose tracking, metric-scale structure perception and globally consistent mapping. We evaluate our approach on both public benchmarks and self-collected datasets, demonstrating substantial improvements in accuracy and robustness over existing visual-centered multi-sensor SLAM systems. The code will be released open-source to support reproducibility and further research¹.

Index Terms—Feed-forward model, multi-sensor fusion, factor graph, SLAM, loop closure

I. INTRODUCTION

Visual SLAM is a widely utilized technique in applications such as robotics, autonomous driving, and extended reality (XR) [1]. SLAM systems generally require comprehensive functionality to support diverse spatial tasks. Compared with 3D reconstruction, visual SLAM places a stronger emphasis on real-time pose estimation and scene structure perception. In contrast to visual odometry, SLAM systems aim to provide a more complete understanding of the environment while simultaneously maintaining long-term global consistency.

Although classical visual SLAM frameworks have achieved notable successes, their practical usability remains limited due

This work was supported by the the National Science Fund for Distinguished Young Scholars of China (42425401), the National Natural Science Foundation of China (423B240), the National Key Research and Development Program of China (2023YFB3907100), and the "Sharp Knife" Technology Research Project of Science and Technology Department of Hubei Province (2023BAA025). (Corresponding author: Xingxing Li.)

The authors are with School of Geodesy and Geomatics, Wuhan University, China (e-mail: xingxingli@whu.edu.cn).

¹<https://github.com/GREAT-WHU/MASt3R-Fusion>

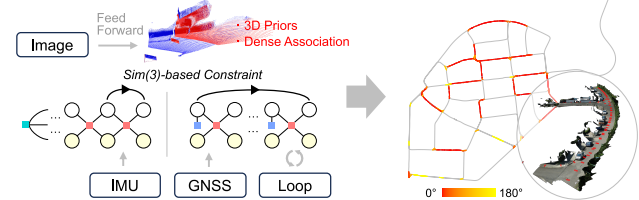


Fig. 1. Illustration of the *MASt3R-Fusion* system. Building upon the 3D perception and data association provided by feed-forward model, this system tightly integrates multi-sensor information (e.g., IMU, GNSS), achieving globally consistent pose estimation and mapping. The heatmap indicates the inter-frame angle of cross-temporal data association. The system is capable of handling arbitrarily long sequences based on **8 GB** GPU memory.

to several critical factors. First, traditional visual SLAM methods based on sparse features or photometric consistency often fail to achieve complete spatial perception, particularly in low-texture environments. Second, the system performance tends to degrade significantly under challenging visual conditions. It also remains an open problem how to achieve life-long consistency across time periods and under varying illumination conditions.

To overcome these limitations, the integration of deep learning/foundation models has emerged as an effective solution [2]. In particular, recent feed-forward neural network-based approaches for visual geometry estimation (e.g., DUS3R [3], MASt3R [4], VGGT [5]), have attracted growing attention. These methods encode the images and decode the latents to directly recover 2D-to-3D pointmaps and other dense information. By leveraging large-scale data to learn spatial priors, they alleviate many of the degeneracies encountered in traditional multi-view stereo (MVS) and SLAM systems, which greatly inspire recent SLAM implementations [6], [7].

Despite significant progress, vision-based methods still suffer from inherent limitations, especially regarding scale consistency and performance degradation in visually deprived environments. To address this, a promising direction is to integrate these novel visual paradigms with complementary sensors, such as inertial measurement units (IMUs) and global navigation satellite system (GNSS), thus to exploit the respective strengths of traditional multi-sensor fusion and learning-based spatial priors.

In this work, we propose *MASt3R-Fusion*, a framework that integrates multi-sensor information with the feed-forward pointmap regression paradigm, facilitating high-functionality SLAM that supports real-time state estimation, complete-view

structure perception and globally consistent mapping.

The contributions of this work are listed as follows:

- 1) We propose a framework to fuse feed-forward pointmap regression with multi-sensor information in a tight way, bridging $\text{Sim}(3)$ -based visual alignment constraints and metric-scale $\text{SE}(3)$ states and factors.
- 2) Based on the feed-forward model, we develop a real-time visual-inertial SLAM system that supports metric-scale pose estimation and dense perception.
- 3) A globally consistent SLAM system that leverages loop closure and GNSS information is developed, in which geometry-based loop closure candidate filtering and full-information iterative optimization are utilized.
- 4) Both public and self-made datasets are employed to comprehensively evaluate the system performance.
- 5) The code is made open-source to benefit the community.

II. RELATED WORK

A. Feed-Forward Pointmap Regression

Since the introduction of DUST3R [3], the feed-forward pointmap regression paradigm has emerged as a prominent research focus in the fields of 3D vision and SLAM. This paradigm enables end-to-end neural networks to directly regress 3D point clouds (pointmaps) from image pairs, thereby overcoming the limitations of traditional multi-view geometry methods, which typically rely on explicit camera parameters and iterative optimization.

Building upon DUST3R, MASt3R [4] introduces several key innovations that address critical bottlenecks, including a descriptor head for refined matching and metric scale inference. Recent improvements to the feed-forward model paradigm include multi-view extensions [5], [8], dynamic scenes [9], permutation equivariance [10], prior information assistance [11], and so on.

B. Deep Visual SLAM

For visual SLAM systems, deep learning has introduced transformative changes beyond the classical implementations [12]. These advancements span both modular improvements, such as enhanced feature matching [13], [14], depth estimation [15], [16], and spatial representations including object-level SLAM [17], [18], renderable neural fields [19], and 3D Gaussian Splatting (3DGS) [20]. In addition, end-to-end approaches have also been explored, where images are directly used as input to estimate outputs such as camera poses and depth maps. Typically, DROID-SLAM [21] achieves an end-to-end SLAM framework by combining dense optical flow with a differentiable dense bundle adjustment (DBA) module. Notably, it retains probabilistic geometric estimation, resulting in high accuracy and robustness.

More recent efforts have focused on incorporating feed-forward neural networks into SLAM pipelines. MASt3R-SLAM [6] builds upon MASt3R's two-view geometry to construct an incremental factor graph, enabling a scalable SLAM system with high-fidelity scene reconstruction. SLAM3R [22]

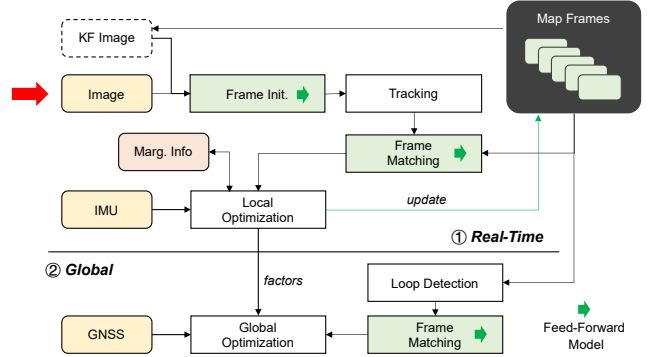


Fig. 2. Flowchart of the system, consisting of real-time SLAM and global optimization stages.

introduces local mapping and global alignment modules, resulting in improved multi-frame scene reconstruction performance. VGGT-SLAM [7] divides sequences into overlapping submaps and globally aligning them on the $\text{SL}(4)$ manifold to better handle projective ambiguity and long video sequences.

C. Multi-Sensor-Aided Visual SLAM

Incorporating multi-sensor information into visual SLAM systems is a common approach to enhance system functionality. A representative example is the integration of visual and inertial data, which enables high-precision, metric-scale pose estimation through filter- or optimization-based information fusion [23], [24]. More advanced methods include photometric-based measurement [25], delayed marginalization [26], and pose-only modeling [27].

When it comes to fusing deep learning-based visual methods with inertial information, SL-SLAM [28] and SuperVINS [29] incorporate learning-based feature modules to improve the visual association. DBA-Fusion [30] fuses the end-to-end trainable DBA with inertial measurements within a factor graph structure. Additionally, some end-to-end methods [31], [32] directly feed both images and inertial data into recurrent neural networks for pose estimation.

Apart from IMU, some methods integrate GNSS information for global functionality [33]–[35]. However, it remains a challenge how to effectively integrate visual(/visual-inertial) information with GNSS for global optimal estimation, as existing methods either focus solely on real-time navigation or rely on pose graph optimization that loses a large amount of visual/inertial information.

In this work, we leverage state-of-the-art feed-forward visual models to formulate visual alignment constraints and design a system that flexibly integrates multi-sensor information. The resulting framework enables real-time, high-precision pose estimation, dense perception and globally consistent mapping.

III. SYSTEM OVERVIEW

The overall system flowchart is illustrated in Fig. 2. The framework is mainly composed of two parts: real-time SLAM and global optimization.

In the real-time SLAM stage, input images are processed through a feed-forward neural network to recover the pointmaps and achieve dense matching. Pose tracking is performed by aligning pointmaps between consecutive frames. A sliding-window factor graph is maintained over a fixed number of keyframes. Sim(3)-based visual constraints among covisible frames are established, while IMU data are tightly incorporated. Probabilistic marginalization is applied to maximize information utilization, which enables high-accuracy pose estimation and metric-scale structure recovery with low-drift performance.

In the global optimization stage, the information stored from real-time SLAM are processed in a global manner with extra loop closures and GNSS information. For loop closure, cross-temporal dense association is achieved through the feed-forward model, which is boosted by geometry-based candidate selection. A global factor graph is employed which incorporates Sim(3)-based visual constraints, IMU pre-integration factors and GNSS position measurements, enabling globally consistent and drift-free pose estimation.

In this system, the feed-forward model introduces two key distinctions from traditional SLAM systems:

- 1) **Powerful 3D priors**, which enable instant access to the scaleless 3D structure information, leading to significant differences in the construction of visual constraints;
- 2) **Aggressive data association**, powered by the 3D awareness, which enables highly effective dense matching to maintain the consistency of visual information under extremely large viewpoints.

These features will be integrated into the probabilistic multi-sensor fusion framework to maximize their potentials.

IV. VISUAL MEASUREMENT BASED ON FEED-FORWARD MODEL

The typical feed-forward visual model directly regresses the 3D pointmaps of RGB images in a common reference frame, and then estimates the camera poses through optimization. This brings about new paradigm for visual-based geometry measurements, rather than relying on bundle adjustment (BA) in traditional SLAM/structure-from-motion (SfM).

In this work, we generally follow the practice in MAS3R-SLAM, using feed-forward pointmap regression with fine-grained matching and Sim(3)-based alignment to construct the visual constraints. Several techniques are used to maximize the geometric accuracy, which would be presented in details.

A. Two-View Feed-Forward Model

Our work uses MAS3R, a typical two-view feed-forward model to process the images, which facilitates pointmap regression and dense data association. The pointmap regression pipeline is depicted in Fig. 3. Firstly, images are encoded into feature tokens following

$$\mathbf{F}_i = \mathcal{F}_{\text{enc}}(\mathbf{I}_i) \quad (1)$$

where \mathbf{F}_i denotes the tokens plus the positional encodings.

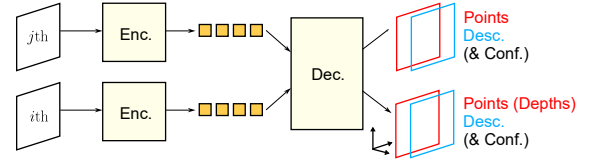


Fig. 3. Illustration of the two-view feed-forward model. Two images are encoded into feature tokens, which are then jointly decoded into two 2D-to-3D pointmaps (with i as the common reference frame), together with two descriptor maps.

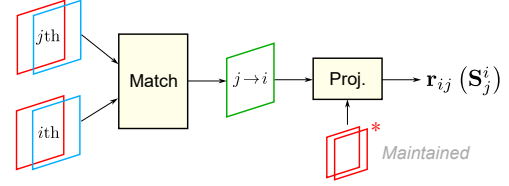


Fig. 4. Illustration of matching process and the construction of visual constraints. Note that the matching process is based on the pointmaps from a temporary two-view feed-forward, whereas the projection residuals are constructed using the pointmaps maintained by the system.

For an image pair (denoted as \mathbf{I}_i and \mathbf{I}_j), their tokens are decoded to produce the pointmaps and descriptors

$$\mathbf{X}_i^{ij}, \mathbf{X}_j^{ij}, \mathbf{D}_i^{ij}, \mathbf{D}_j^{ij} = \mathcal{F}_{\text{dec}}(\mathbf{F}_i, \mathbf{F}_j) \quad (2)$$

where superscript “ ij ” indicates the asymmetric two-view relationship, $\mathbf{X}_i^{ij}, \mathbf{X}_j^{ij}$ with $(H \times W, 3)$ shapes are 2D-to-3D pointmaps described in the reference frame i , $\mathbf{D}_i^{ij}, \mathbf{D}_j^{ij}$ with $(H \times W, D)$ shapes are pixel-level descriptor maps for further fine-grained association.

Thanks to large-scale training and the learning capability of transformers, the pointmap regression paradigm has been demonstrated to be highly effective. Essentially, the model integrates 3D spatial geometric priors with two-view stereo to produce reasonable structure information in various conditions.

As the regressed pointmaps are described in the unified reference frame i , dense matching based on ray proximity can be achieved through the following optimization

$$\hat{\mathbf{u}}_j^i = \arg \min_{\mathbf{u}_j^i} \left\| \frac{\mathbf{X}_i^{ij}[\mathbf{u}_j^i]}{\|\mathbf{X}_i^{ij}[\mathbf{u}_j^i]\|} - \frac{\mathbf{X}_j^{ij}}{\|\mathbf{X}_j^{ij}\|} \right\|^2 \quad (3)$$

where \mathbf{u}_j^i with $(H \times W, 2)$ shape denotes the 2D coordinates on image i associated with the grid points on image j , “[.]” denotes retrieving the value at the corresponding 2D index on the pointmap. Here, bilinear interpolation is utilized for the retrieval, and the gradient map of \mathbf{X}_i^{ij} is used for efficient optimization. After the optimization based on ray proximity, awareness of the 3D structure can help eliminate dynamic points (with large depth residuals).

As pointed by [4], geometry-based matching can be further improved by taking into account the feature-based refinement, which utilizes the descriptor maps following

$$(\hat{\mathbf{u}}_j^i)' = \arg \max_{\mathbf{u}_j^i} d(\mathbf{D}_i^{ij}[\mathbf{u}_j^i], \mathbf{D}_j^{ij}) \quad (4)$$

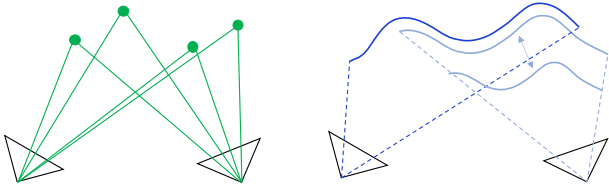


Fig. 5. Illustration different forms of visual constraints. **Left:** bundle adjustment, in which landmarks and camera poses are jointly optimized with little prior knowledge. **Right:** Pointmap alignment, in which camera poses and pointmap scales are optimized, built upon the knowledge of the scaleless 3D structure.

where $d(\cdot, \cdot)$ denotes the dot-product. As the channel number of \mathbf{D} is large and the descriptor lacks smoothness, a neighborhood searching (taking $\hat{\mathbf{u}}_j^i$ as initials) rather than optimization is utilized to obtain $(\hat{\mathbf{u}}_j^i)'$.

To achieve sub-pixel data association, we asymmetrically upsample \mathbf{D}_j^{ij} through bilinear interpolation

$$\mathbf{D}_{j,\text{up}}^{ij} = \text{Upsample}_{\text{bilinear}}(\mathbf{D}_j^{ij}, \text{scale} = 4) \quad (5)$$

then perform the refinement around $(\hat{\mathbf{u}}_j^i)'$, following

$$(\hat{\mathbf{u}}_j^i)'' = \arg \max_{\mathbf{u}_j^i} d\left(\mathbf{D}_{j,\text{up}}^{ij}[\mathbf{u}_j^i], \mathbf{D}_i^{ij}\right) \quad (6)$$

which contributes to better accuracy for SLAM tasks.

B. Visual Constraint based on Pointmap Alignment

Considering multiple frames of images, we maintain both the pointmaps and their associated poses, represented as

$$\mathcal{K} = \{(\mathbf{X}_i, \mathbf{S}_i) \mid i = 0, 1, \dots, K\}, \quad (7)$$

where \mathbf{X}_i denotes the pointmap of frame i , and

$$\mathbf{S}_i = \begin{bmatrix} s\mathbf{R} & \mathbf{t} \\ 0 & 1 \end{bmatrix} \in \text{Sim}(3) \quad (8)$$

is the camera-to-world Sim(3) transformation. Here, \mathbf{S}_i first scales the points to a unified scale and then transforms them into the world coordinate frame.

The self-referenced pointmap \mathbf{X}_i is initialized using the two-view feed-forward results from Eq. (2), following

$$\mathbf{X}_i \leftarrow \mathbf{X}_i^{ij} \quad (9)$$

in which frame j is generally the last keyframe.

Specifically, assuming known camera intrinsics, the 3D points can be constrained to lie along their corresponding rays

$$\mathbf{X}_i \leftarrow \pi(\mathbf{u}_i, (\mathbf{X}_i)_z) \quad (10)$$

where \mathbf{u}_i are the grid-like pixel coordinates, $(\mathbf{X}_i)_z$ is the depth vector, $\pi(\cdot)$ is the camera projection model, whose inverse operation backprojects 2D pixels to 3D points.

Although feed-forward reconstruction is considered advantageous in that it obviates the requirement for camera parameters, in practice we found that camera distortions can introduce considerable instability. Therefore, we consider the case where the camera parameters are known.

Based on the dense association \mathbf{u}_j^i produced by two-view matching, we can align two pointmaps and construct the following residuals

$$\mathbf{r}_{ij}(\mathbf{S}_j^i) = \left[\begin{array}{l} \mathbf{u}_j^i - \pi(\mathbf{S}_j^i \circ \mathbf{X}_j) \\ (\mathbf{X}_i[\mathbf{u}_j^i])_z - (\mathbf{S}_j^i \circ \mathbf{X}_j)_z \end{array} \right] \quad (11)$$

where “ \circ ” denotes the transforming operation. The residuals in the upper part resemble the reprojection error with known depth and play a dominant role, whereas the residuals in the lower part are primarily used to handle pure rotation cases.

The inter-frame transformation can be directly estimated based on the above pointmap alignment residuals

$$\hat{\mathbf{S}}_j^i = \arg \min_{\mathbf{S}_j^i} \|\mathbf{r}_{ij}(\mathbf{S}_j^i)\|_{\mathbf{Q}_{ij}}^2 + \|\mathbf{r}_{ji}(\mathbf{S}_i^j)\|_{\mathbf{Q}_{ji}}^2 \quad (12)$$

where bi-directional projections are considered, \mathbf{Q}_{ij} , \mathbf{Q}_{ji} are the weighting factors which consider network-outputs confidence and Huber robust kernel function. This is used for pose tracking of a new frame.

It is noted that, the residual computation and the optimization process are dense due to the large number of pixels. Therefore, both the residuals and the Hessian information for each projection are computed on GPU. To be specific, the Hessian information is computed following

$$\mathbf{r}_{ij} = \mathbf{J}_{ij}^r \boldsymbol{\eta}_j^i \quad (13)$$

$$\underbrace{(\mathbf{J}_{ij}^r)^\top \mathbf{r}_{ij}}_{\mathbf{v}_{ij}} = \underbrace{(\mathbf{J}_{ij}^r)^\top \mathbf{J}_{ij}^r}_{\mathbf{H}_{ij}} \boldsymbol{\eta}_j^i \quad (14)$$

where $\boldsymbol{\eta}_j^i \in \mathbb{R}^7$ is the Lie algebra, \mathbf{J}_{ij}^r is the \mathbf{r}_{ij} -to- \mathbf{S}_j^i Jacobian. After GPU processing, the Hessian-form information $(\mathbf{H}_{ij}, \mathbf{v}_{ij})$ are in compact $(7, 7)$ and $(7, 1)$ shapes and can be processed efficiently on CPU.

When multiple frames within a neighborhood are considered, residuals can be constructed for multiple image pairs, thereby enabling joint estimation of multi-frame poses and scales

$$\{\hat{\mathbf{S}}\} = \arg \min_{\{\mathbf{S}\}} \sum_{(i,j) \in \mathcal{E}} \|\mathbf{r}_{ij}(\mathbf{S}_i, \mathbf{S}_j)\|_{\mathbf{Q}_{ij}}^2 \quad (15)$$

where \mathcal{E} is the set of valid two-view projections. During the optimization, local-to-global Jacobians $\mathbf{J}_{(i,j)}^{ij} \in \mathbb{R}^{7 \times 14}$ are optimized.

In contrast to BA commonly used in vision-based methods that jointly estimate point depths and camera poses, the above-described visual measurement model does not include point depths, and instead builds relatively independent constraints between pairwise images. This greatly simplifies the formulation of the problem, which is made possible by the strong capability of the visual foundation model to provide accurate estimates of 3D scene structure (up to a certain scale).

For comparison, we revisit the widely used BA technique and the re-projection error formula, as shown below

$$\mathbf{r}_{ij}(\mathbf{T}_j^i, \mathbf{d}_j) = [\mathbf{u}_j^i - \pi(\mathbf{T}_j^i \circ \pi^{-1}(\mathbf{u}_j, \mathbf{d}_j))] \quad (16)$$

$$\{\hat{\mathbf{T}}, \hat{\mathbf{d}}\} = \arg \min_{\{\mathbf{T}, \mathbf{d}\}} \sum_{i,j \in \mathcal{K}} \|\mathbf{r}_{ij}(\mathbf{T}_i, \mathbf{T}_j, \mathbf{d}_j)\|_{\mathbf{Q}_{ij}}^2 \quad (17)$$

where \mathbf{d}_j are the depths of landmarks in the source frame j , \mathbf{u}_j are the pixel coordinates.

It can be seen that when BA constructs visual constraints, it relies on the parameterization of a large number of point depths \mathbf{d}_j ; this greatly increases the scale of the problem and needs careful initialization for good convergence. For better efficiency, a two-step optimization can be adopted by eliminating landmarks first through Schur complement and then constructing pose constraints [36]. However, this process involves all frames related to \mathbf{d}_j , making the construction of visual constraints less flexible. These issues no longer exist in pointmap-alignment-based visual constraints, which can be easily modeled as pairwise residuals.

It is noted that, this advantage relies on the assumption that the pointmap structure is accurate and scale is the only uncertain factor. Thanks to the spatial awareness of the feed-forward model, this assumption generally holds. Yet, under specific conditions, significant errors may be introduced—particularly when the points appear very far in image j but very close in image i . In such cases, the depth uncertainty of the points in image j will have a pronounced impact (large disparities) in image i . This issue is not obvious in small-scale scenes, but becomes significant in large-scale outdoor environments, typically for the long-time forward-moving scenario.

To mitigate the influence of this uncertainty, we simply apply a mask to downweight the residuals in the above mentioned projection process, as shown below

$$\mathbf{r}_{ij}[\text{mask}] = \mathbf{r}_{ij}[\text{mask}] \cdot f_{\text{downweight}} \quad (18)$$

$$\text{mask} = (\mathbf{S}_j^i \circ \mathbf{X}_j)_z < \tau \cdot (\mathbf{X}_i)_z \quad (19)$$

where $f_{\text{downweight}}$ is a downweight factor (e.g., 0.1), τ is an empirical threshold (e.g., 1.25).

This simple mechanism helps fully leverage 3D prior information while mitigating errors caused by unideal conditions, thereby contributing to the overall accuracy of the SLAM system.

V. REAL-TIME SLAM

Based on the above paradigm, visual alignment constraints operate independently on a frame-to-frame basis, involving only a very compact set of associated parameters. Beyond the shared common parameters, there exist no functional dependencies among distinct visual constraints. This characteristic enables highly flexible and modular construction of factor graphs. Nevertheless, several issues need to be addressed:

- 1) Visual constraints are formulated on the Sim(3) group, whereas measurements from IMU (and other sensors) are generally defined on SE(3), necessitating appropriate adaptation between these representations.
- 2) Visual constraints are constructed densely using float32 precision with GPU acceleration. However, float32 precision is insufficient to accurately represent poses at large scales.
- 3) The dense visual constraint construction depends on the global poses defined in Sim(3). If not carefully handled, the factor graph information would change with shifts

of the reference frame, leading to more significant linearization error and inflexibility of global/multi-session optimization.

In this section, we construct a sliding-window-based real-time SLAM pipeline, during which the above issues are taken into consideration.

A. Isomorphic Group Transformation

To bridge the gap between Sim(3)-based visual alignment constraints and a more common metric-scale SE(3) factor graph, we introduce the isomorphic group transformation.

A Sim(3)-based similarity transformation can be described as

$$\mathbf{S} \circ \mathbf{p} = \underbrace{\begin{bmatrix} s\mathbf{R} & \mathbf{t} \\ 0 & 1 \end{bmatrix}}_{\mathbf{S} \in \text{Sim}(3)} \begin{bmatrix} \mathbf{p} \\ 1 \end{bmatrix}, \quad (20)$$

where $s \in \mathbb{R}^+$ denotes the scale, $\mathbf{R} \in \text{SO}(3)$ the rotation, and $\mathbf{t} \in \mathbb{R}^3$ the translation.

Equivalently, the same transformation can be factorized into an SE(3) transform followed by a scalar scaling:

$$\mathbf{T} \circ s \circ \mathbf{p} = \underbrace{\begin{bmatrix} \mathbf{R} & \mathbf{t} \\ 0 & 1 \end{bmatrix}}_{\mathbf{T} \in \text{SE}(3)} \underbrace{\begin{bmatrix} s & 0 \\ 0 & 1 \end{bmatrix}}_{\text{scaling}} \begin{bmatrix} \mathbf{p} \\ 1 \end{bmatrix} \quad (21)$$

Thus the similarity group Sim(3) can be equivalently represented in an isomorphic form as the product space $\text{SE}(3) \times \mathbb{R}$:

$$\mathbf{S} \in \text{Sim}(3), \quad (\mathbf{T}, s) \in \text{SE}(3) \times \mathbb{R} \quad (22)$$

By introducing Lie algebras and perturbations, we obtain the following relationship:

$$\mathbf{S} \boxplus \boldsymbol{\eta} = (\mathbf{T} \boxplus \boldsymbol{\xi}) \circ (s + \delta s) \quad (23)$$

where

$$\boldsymbol{\eta} = \begin{bmatrix} \boldsymbol{\omega} \\ \boldsymbol{\nu} \\ \sigma \end{bmatrix}_{7 \times 1}, \quad \boldsymbol{\xi} = \begin{bmatrix} \boldsymbol{\theta} \\ \boldsymbol{\tau} \end{bmatrix}_{6 \times 1} \quad (24)$$

with $\boldsymbol{\omega}, \boldsymbol{\theta} \in \mathbb{R}^3$ denoting rotation perturbations, $\boldsymbol{\nu}, \boldsymbol{\tau} \in \mathbb{R}^3$ denoting translation perturbations, and $\sigma, \delta s \in \mathbb{R}$ representing scale perturbations.

On this basis, we can derive the linear transformation relationship between the Lie algebras:

$$\begin{bmatrix} s\mathbf{R} & \mathbf{t} \\ 0 & 1 \end{bmatrix} \begin{bmatrix} \boldsymbol{\omega}^\wedge + \sigma \mathbf{I} & \boldsymbol{\nu} \\ 0 & 1 \end{bmatrix} = \begin{bmatrix} \mathbf{R} & \mathbf{t} \\ 0 & 1 \end{bmatrix} \begin{bmatrix} \boldsymbol{\theta}^\wedge & \boldsymbol{\tau} \\ 0 & 1 \end{bmatrix} \begin{bmatrix} s + \delta s & 0 \\ 0 & 1 \end{bmatrix} \quad (25)$$

This leads to the following compact relation:

$$\begin{bmatrix} \boldsymbol{\omega} \\ \boldsymbol{\nu} \\ \sigma \end{bmatrix} = \underbrace{\begin{bmatrix} 1 & & \\ & s\mathbf{I} & \\ & & s \end{bmatrix}}_{\boldsymbol{\Lambda}} \begin{bmatrix} \boldsymbol{\theta} \\ \boldsymbol{\tau} \\ \delta s \end{bmatrix} \quad (26)$$

where $\boldsymbol{\Lambda}$ denotes the diagonal scaling transformation between the two Lie algebra representations.

By introducing this transformation, Sim(3)-based visual constraints can be consistently applied to SE(3) poses, enabling joint optimization with IMU, GNSS, and other metric-scale sensor information.

B. Multi-Sensor Factor Graph

In the real-time SLAM stage, we maintain a sliding-window system state as follows

$$\mathcal{X} = \{\mathcal{X}_i \mid i \in \mathcal{W} = \{K - N + 1, \dots, K\}\}, \quad (27)$$

$$\mathcal{X}_i = (\mathbf{T}_i, s_i, \mathbf{v}_i, \mathbf{b}_i) \quad (28)$$

where N is the fixed size of the sliding window, and K denotes the index of the latest keyframe, $\mathbf{T}_i \in \text{SE}(3)$ is the camera pose (rotation and translation) of the i -th keyframe, $s_i \in \mathbb{R}$ is the scale parameter, $\mathbf{v}_i \in \mathbb{R}^3$ is the body velocity in the world frame, $\mathbf{b}_i = (\mathbf{b}_i^g, \mathbf{b}_i^a)$ is the IMU bias vector, including gyroscope bias $\mathbf{b}_i^g \in \mathbb{R}^3$ and accelerometer bias $\mathbf{b}_i^a \in \mathbb{R}^3$. It should be noted that all states are maintained in double precision (float64).

For visual information, a quadric-form factor is utilized, following

$$\mathbf{E}_v(\mathcal{X}_i, \mathcal{X}_j) = \frac{1}{2} l_v(\mathcal{X})^\top \mathbf{H}_{v,ij} l_v(\mathcal{X}) - l_v(\mathcal{X})^\top \mathbf{v}_{v,ij} \quad (29)$$

$$\begin{cases} \mathbf{H}_{v,ij} = \mathbf{\Lambda}_{(i,j)}^\top \mathbf{J}_{(i,j)}^{ij} \mathbf{J}_{(i,j)}^{ij} \mathbf{\Lambda}_{(i,j)} \\ \mathbf{v}_{v,ij} = \mathbf{\Lambda}_{(i,j)}^\top \mathbf{J}_{(i,j)}^{ij} \mathbf{v}_{ij} \end{cases} \quad (30)$$

where $(\mathbf{H}_{ij}, \mathbf{v}_{ij})$ is the Hessian information of the Sim(3)-based visual constraint (Eq. (14)), $(\mathbf{H}_{v,ij}, \mathbf{v}_{v,ij})$ is the Hessian information after local-to-global transformation (through Jacobian $\mathbf{J}_{(i,j)}^{ij}$) and isomorphic group transformation, $l_v(\cdot)$ is the linear container that transform current state \mathcal{X} to the Lie algebras at the linearization point in Eq. (11).

When constructing visual information, we first obtain the relative Sim(3) transformation between projection frames using the maintained double-precision (float64) poses and scales. The Hessian information $(\mathbf{H}_{ij}, \mathbf{v}_{ij})$ is then computed using Eq. (11) and (14) in single precision (float32), and subsequently transformed via a double-precision linear mapping (Eq. (30)) into constraints on the global parameters. By restricting single-precision GPU computation within the local scale, this strategy mitigates numerical instabilities in large-scale scenarios.

Besides, as we use right-hand perturbations, the Jacobians \mathbf{J}_{ij}^r and $\mathbf{J}_{(i,j)}^{ij}$ are only related to the relative transformation \mathbf{S}_j^i and regardless of the global reference. This contributes to lower error during marginalization and enables more flexible use of the factors in global/multi-session optimization.

For IMU information, the classic IMU pre-integration [37] is used for state prediction and inter-frame constraints

$$\mathbf{r}_b(\mathcal{X}_k, \mathcal{X}_{k+1}) = \begin{bmatrix} \mathbf{R}_{b_k}^w \top \left(\mathbf{p}_{b_{k+1}}^w - \mathbf{p}_{b_k}^w + \frac{1}{2} \mathbf{g}^w \Delta t_k^2 - \mathbf{v}_{b_k}^w \Delta t_k \right) - \Delta \tilde{\mathbf{p}}_{b_{k+1}}^{b_k} \\ \mathbf{R}_{b_k}^w \top \left(\mathbf{v}_{b_{k+1}}^w + \mathbf{g}^w \Delta t_k - \mathbf{v}_{b_k}^w \right) - \Delta \tilde{\mathbf{v}}_{b_{k+1}}^{b_k} \\ \text{Log} \left((\mathbf{R}_{b_k}^w)^{-1} \mathbf{R}_{b_{k+1}}^w \left(\Delta \tilde{\mathbf{R}}_{b_{k+1}}^{b_k} \right)^{-1} \right) \\ \mathbf{b}_{k+1}^a - \mathbf{b}_k^a \\ \mathbf{b}_{k+1}^g - \mathbf{b}_k^g \end{bmatrix} \quad (31)$$

where $\Delta \tilde{\mathbf{p}}_{b_{k+1}}^{b_k}$, $\Delta \tilde{\mathbf{v}}_{b_{k+1}}^{b_k}$, $\Delta \tilde{\mathbf{R}}_{b_{k+1}}^{b_k}$ are the IMU preintegration terms [37], \mathbf{g}^w is the gravity vector, Δt_k is the time interval. Considering the difference between the camera pose and the

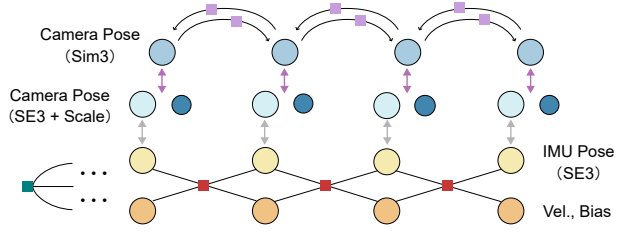


Fig. 6. Illustration of the sliding-window factor graph in the real-time SLAM stage. The Sim(3)-to-SE(3) isomorphic group transformation and IMU-camera extrinsic transformation are used to bridge the gap between visual constraints and inertial information. Probabilistic marginalization is employed for optimal information utilization with controlled problem scale. For clarity, only the adjacent visual constraints are shown.

IMU pose, the extrinsic parameters need to be taken into account, as shown in the following equation

$$\mathbf{T}_{b_i}^w = \mathbf{T}_i \circ \mathbf{T}_c^{b_i} \quad (32)$$

where $\mathbf{T}_c^b \in \text{SE}(3)$ is the IMU-camera extrinsic transformation.

The fusion of visual and IMU information forms the fundamental mechanism of visual-inertial odometry (VIO), which can provide metric-scale information, low-drift pose estimation, and gravity awareness. To maximize the performance of this mechanism, probabilistic marginalization needs to be considered. To be specific, When the number of states within the sliding window exceeds N , a local factor graph associated with the oldest pose is constructed. The state at the oldest time step is then eliminated via the Schur complement [23], thereby yielding the marginalization information $(\mathbf{H}_m, \mathbf{v}_m)$. This leads to the following quadric-form factor

$$\mathbf{E}_m(\mathcal{X}) = \frac{1}{2} l_m(\mathcal{X})^\top \mathbf{H}_m l_m(\mathcal{X}) - l_m(\mathcal{X})^\top \mathbf{v}_m \quad (33)$$

where $l_m(\cdot)$ is the linear container that transform the current states \mathcal{X} to the Lie algebras at the linearization point of marginalization.

Thus, the cost function corresponding to the real-time visual-inertial SLAM system is described as

$$\sum_{i \in \mathcal{W}} \|\mathbf{r}_b(\mathcal{X}_i, \mathcal{X}_{i+1})\|^2 + \sum_{(i,j) \in \mathcal{E}} \mathbf{E}_v(\mathcal{X}_i, \mathcal{X}_j) + \mathbf{E}_m(\mathcal{X}) \quad (34)$$

With the sliding-window setup, the scale of this optimization problem is kept small, and the system is free from the frequent re-computation of old projections. The computational load is mainly concentrated in the feed-forward model. The effective integration of V-I information allows the system to achieve high-precision pose/scale estimation using only local dense matching, enabling real-time operation on a 4080 laptop. Furthermore, the sliding-window design allows the system to handle arbitrarily long data sequences while requiring only **8 GB** of GPU memory.

VI. GLOBAL SLAM

During the real-time SLAM stage, the V-I information (feature tokens $\{\mathbf{F}\}$, pointmaps $\{\mathbf{X}\}$, system states $\{\mathcal{X}\}$, Hessian-form visual information $\{\mathbf{H}, \mathbf{v}\}$ and IMU factors) is logged to the file.

In the global SLAM process, based on the pre-processed V-I information and state estimation from the real-time stage, we incorporate loop closure and GNSS data to achieve consistent pose estimation and mapping through efficient global optimization.

A. Loop Closure

Loop closure detection is crucial for achieving consistent mapping and drift-free pose estimation in GNSS-denied environments. In particular, the feed-forward visual model provides the fundamental capability for data association across large viewpoints, making it especially worthy of attention.

First, as proposed in [6], we can use image feature tokens obtained from the feed-forward encoder to construct an image retrieval system

$$\mathbf{d}_i = \mathcal{F}_{\text{ret}}(\mathbf{F}_i) \quad (35)$$

$$p_q^* = \arg \min_p \|\mathbf{d}_p - \mathbf{d}_q\| \quad (36)$$

where \mathbf{d}_i is the descriptor vector, p_q^* is the retrieved index by query q . Considering the need for cross-temporal loop closure, we select the top-10 indices and exclude temporally consecutive frames from them, thereby constructing the loop closure candidate set.

Benefiting from the strong association capability of the feed-forward model, this system is highly effective to recognize subtle cues of a common scene, but also produces a considerable number of false positives. A further dense matching step can be used for verification of the loop closure, while this can introduce significant extra computational cost.

To lower the risk caused by false loop closures and to reduce the computational cost of fine-grained verification, an adaptive filtering mechanism would be beneficial. Building on the low-drift pose estimates provided by VIO, we developed a highly efficient method to eliminate redundant false detections based on pose uncertainty, which reduces redundancy while preserving as many aggressive loop closure candidates as possible.

Based on the odometry essence of VIO, we simplify the position estimation as a Markov process, leading to the following expression

$$\Delta \hat{\mathbf{p}}_{p,q}^w = \sum_p^{q-1} \Delta \hat{\mathbf{p}}_{i,i+1}^w \quad (37)$$

where $\Delta \hat{\mathbf{p}}_{p,q}^w$ is the relative translation estimation between timestamp p and q . Considering the practical need of loop closure, we simplify the translation into 2D horizontal movement.

Considering the error of the odometry, we get

$$\Delta \hat{\mathbf{p}}_{i,i+1}^w = \Delta \mathbf{p}_{i,i+1}^w + \epsilon_{i,i+1}, \quad (38)$$

where $\epsilon_{i,i+1}$ is the estimation error, modeled as a random variable conforming to a certain uncertainty.

By dividing the odometry uncertainty into “along” direction (corresponding to scale error) and “cross” direction (corresponding to heading error), we can estimate the translation uncertainty following

$$\epsilon_{i,i+1} \sim \mathcal{N}(\mathbf{0}, d^2 \mathbf{Q}), \quad (39)$$

where $d = \|\Delta \hat{\mathbf{p}}_{i,i+1}^w\|$ is the translation distance, \mathbf{Q} is a direction-and-uncertainty-related ellipsoid, following

$$\mathbf{Q} = \sigma_d^2 \mathbf{P}_{\parallel} + \sigma_n^2 \mathbf{P}_{\perp} \quad (40)$$

$$\begin{cases} \mathbf{P}_{\parallel} = \mathbf{n} \mathbf{n}^{\top} \\ \mathbf{P}_{\perp} = \mathbf{I} - \mathbf{n} \mathbf{n}^{\top} \\ \mathbf{n} = \Delta \hat{\mathbf{p}}_{i,i+1}^w / \|\Delta \hat{\mathbf{p}}_{i,i+1}^w\| \end{cases} \quad (41)$$

where σ_d is the uncertainty factor related to the scale error of translation, σ_n is the uncertainty factor related to the direction/heading.

Based on the above equations, we can efficiently compute the covariances of $\epsilon_{i,i+1}$, and estimate the covariance of inter-frame translation $\Delta \hat{\mathbf{p}}_{p,q}^w$ by summing up. This operation is fast by utilizing vectorization. Afterwards, we turn the uncertainty of translation into the uncertainty of inter-frame distance

$$\sigma_{p,q} = \sqrt{\frac{\Delta \hat{\mathbf{p}}_{p,q}^w \top \mathbf{Q}_{p,q} \Delta \hat{\mathbf{p}}_{p,q}^w}{\|\Delta \hat{\mathbf{p}}_{p,q}^w\|^2}}, \quad (42)$$

where $\mathbf{Q}_{p,q}$ is the estimated covariance of translation $\Delta \hat{\mathbf{p}}_{p,q}^w$.

Equation (42) forms a 2D uncertainty map of inter-frame distances. It should be noted that, when predicting the co-visibility, we need to consider not only the spatial proximity of camera positions. Due to the presence of large-angle loop closures, co-visible frames may observe the same scene while exhibiting significant positional differences caused by varying viewpoints. Therefore, it is more important to focus on the proximity of observed points. To this end, we approximate the main observation point of a camera frame i by introducing a point of interest, defined as

$$\mathbf{p}_{o,i} = \left(\mathbf{T}_i \circ \begin{bmatrix} 0 \\ 0 \\ L \end{bmatrix} \right)_{x,y} \quad (43)$$

where L denotes the median scene depth of the corresponding camera frame.

A heuristic criterion for selecting co-visible frames is given as:

$$d(\mathbf{p}_{o,q}, \mathbf{p}_{o,p}) < L \quad (44)$$

The next task is to determine, based on positional uncertainty, whether there is a possibility that two frames satisfy condition (44). By approximating the uncertainty of the distance between points $\mathbf{p}_{o,p}$ and $\mathbf{p}_{o,q}$ to that of the distance between points \mathbf{p}_p and \mathbf{p}_q , the probability distribution function corresponding to the above condition can be obtained

$$P(d(\hat{\mathbf{p}}_{o,q}, \hat{\mathbf{p}}_{o,p}) < L) = \Phi\left(\frac{L - d(\hat{\mathbf{p}}_{o,q}, \hat{\mathbf{p}}_{o,p})}{\sigma_{p,q}}\right) \quad (45)$$

where $\Phi(\cdot)$ denotes the standard normal cumulative distribution function (CDF).

On this basis, we take the following criterion to select possible loop closure candidates

$$d(\hat{\mathbf{p}}_{o,q}, \hat{\mathbf{p}}_{o,p}) < L + \sigma_{p,q} \quad (46)$$

which corresponds to a relatively strict 15.87% tailed probability to exclude cases that don't satisfy condition (44).

A example of the candidate filtering is presented in Fig. 7.

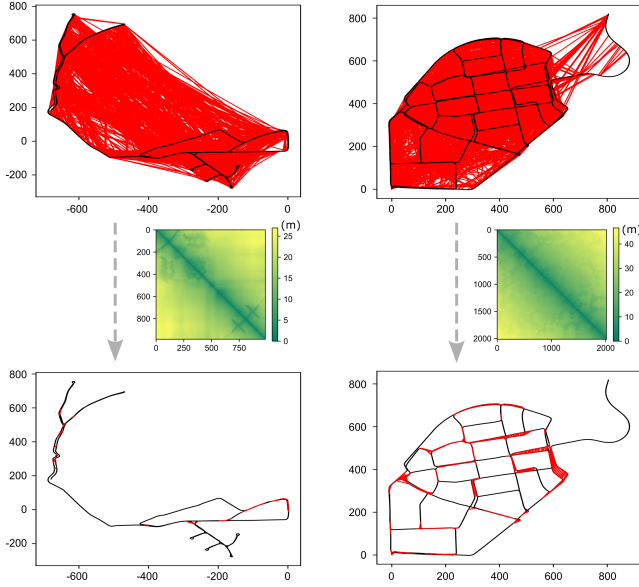


Fig. 7. Loop closure candidate filtering based on efficient positional uncertainty evaluation. The upper figure illustrates the set of loop closure candidates selected based on the similarity scores and temporal non-contiguity. After filtering with the distance uncertainty matrix $\sigma_{p,q}$, the lower figure presents the geometrically feasible loop closure candidates.

B. Global Factor Graph Optimization

Building upon the above work, the global graph integrates GNSS, loop closure and local constraints for optimal estimation, and leverages sparsity to enable efficient optimization.

For visual loop closure measurements, the relative pose estimate between loop closure frame (i, j) can be directly obtained through the projection between two frames (Eq. (12)), which is $\tilde{\mathbf{S}}_{j,\text{loop}}^i$. With the knowledge of s_i obtained in the real-time SLAM stage, the SE(3) relative pose can be retrieved, which leads to a metric-scale relative pose constraint

$$\mathbf{r}_r(\mathcal{X}_i, \mathcal{X}_j) = \mathbf{T}_i \circ \mathbf{T}_j^{-1} \circ \tilde{\mathbf{T}}_{j,\text{loop}}^i \quad (47)$$

where $\tilde{\mathbf{T}}_{j,\text{loop}}^i$ is the estimated relative pose between the loop closure frames.

For more accurate constraints, we also extract the Hessian-form information $(\mathbf{H}_{ij,\text{loop}}, \mathbf{v}_{ij,\text{loop}})$, $(\mathbf{H}_{ji,\text{loop}}, \mathbf{v}_{ji,\text{loop}})$ during the estimation of $\tilde{\mathbf{S}}_{j,\text{loop}}^i$.

For GNSS measurements, the residual is described as follows:

$$\mathbf{r}_g(\mathcal{X}_i) = \mathbf{T}_w^n \circ \mathbf{T}_i \circ \mathbf{T}_c^b \circ \mathbf{t}_g^c - \tilde{\mathbf{p}}_{g,i}^n \quad (48)$$

where $\tilde{\mathbf{p}}_{g,i}^n$ is the measured position of the GNSS phase center in the navigation frame, \mathbf{t}_g^b is the IMU-GNSS lever-arm, \mathbf{T}_w^n is a fixed world-to-navigation transformation obtained through the initial alignment. To overcome the time asynchrony between GNSS measurements and keyframes, we introduce a temporary pre-integration term to bridge the GNSS measurement with the nearest keyframe timestamp. Thus, the combined cost function will be:

$$\|\mathbf{r}_g(\mathcal{X}_i, \text{sync})\|^2 + \|\mathbf{r}_b(\mathcal{X}_i, \mathcal{X}_i, \text{sync})\|^2 \quad (49)$$

where $\mathcal{X}_i, \text{sync}$ is a temporary node extended from \mathcal{X}_i based on IMU data.

During global optimization, due to the inconsistency between odometry poses and loop closure relative poses, directly using the Hessian-form loop information for optimization is ineffective (since the initial estimate deviates from the linearization point when estimating $\tilde{\mathbf{S}}_{j,\text{loop}}^i$). Therefore, in the global pose graph, we first introduce loop closure constraints in the form of relative poses (47). The resulting optimization problem is formulated as follows:

$$\begin{aligned} \min \sum_{i \in \mathcal{K}} \|\mathbf{r}_b(\mathcal{X}_i, \mathcal{X}_{i+1})\|^2 + \sum_{(i,j) \in \mathcal{E}} \mathbf{E}_v(\mathcal{X}_i, \mathcal{X}_j) \\ + \sum_{(i,j) \in \mathcal{L}} \rho_C(\|\mathbf{r}_r(\mathcal{X}_i, \mathcal{X}_j)\|^2) \\ + \sum_{i \in \mathcal{K}} \|\mathbf{r}_b(\mathcal{X}_i, \mathcal{X}_{i,\text{sync}})\|^2 + \rho_C(\|\mathbf{r}_g(\mathcal{X}_{i,\text{sync}})\|^2) \end{aligned} \quad (50)$$

where \mathcal{L} is the loop closure set. In the above optimization process, a Cauchy robust kernel function $\rho_C(\cdot)$ is applied to the loop closure constraints to mitigate the influence of incorrect loop closures. After obtaining a reliable global pose estimate, we convert the inlier loop closure constraints into the Hessian form and optimize the following more fundamental optimization problem as follows:

$$\begin{aligned} \min \sum_{i \in \mathcal{K}} \|\mathbf{r}_b(\mathcal{X}_i, \mathcal{X}_{i+1})\|^2 + \sum_{(i,j) \in \mathcal{E}} \mathbf{E}_v(\mathcal{X}_i, \mathcal{X}_j) \\ + \sum_{(i,j) \in \mathcal{L}'} \mathbf{E}_v(\mathcal{X}_i, \mathcal{X}_j) \\ + \sum_{i \in \mathcal{K}} \|\mathbf{r}_b(\mathcal{X}_i, \mathcal{X}_{i,\text{sync}})\|^2 + \rho_C(\|\mathbf{r}_g(\mathcal{X}_{i,\text{sync}})\|^2) \end{aligned} \quad (51)$$

where \mathcal{L}' is the inlier loop closure set.

It is noted that during global optimization, the Hessian information $(\mathbf{H}_{ij}, \mathbf{v}_{ij})$ with respect to the relative transformation \mathbf{S}_j^i in Eq. (30) doesn't need to be re-computed through direct projection Eq. (11), as the relative transformation is stable. Only the local-to-global linear mapping (Eq. (30)) needs to be iteratively performed, which makes the optimization highly efficient while keep the accurate visual information.

Through the stepwise optimization strategy and the precise utilization of measurement information, the global optimization problem can be solved efficiently while naturally detecting and mitigating outliers in GNSS and loop closure measurements in a probabilistic manner, thereby achieving nearly optimal estimation results. In contrast, traditional global fusion methods based solely on pose graphs discard the original IMU and visual information, causing inaccurate VIO pose estimates to significantly affect the global estimation, particularly with respect to scale uncertainty.

VII. EXPERIMENTS

In the experimental section, we first evaluate the performance of the visual-inertial integration on the public KITTI-360 [38] and SubT-MRS [39] datasets, including both the real-time SLAM and global optimization stages. Subsequently, we assess the performance of the visual-inertial-GNSS fusion on our self-collected Wuhan urban dataset. Monocular camera information is used for all the tests.

A. KITTI-360 Dataset

KITTI-360 [38] is a multi-sensor dataset for autonomous-driving-related benchmarking, which consists of multiple relatively long (kilometer-level) data sequences. The data scenarios include residential areas and highways. We mainly utilize the front-facing monocular camera and the IMU data for the test.

Firstly, we test the performance of real-time VIO. For comparison, multiple state-of-the-art monocular VIO schemes are considered, including feature-based methods (VINS-Fusion [34], ORB-SLAM3 [12]), direct methods (DM-VIO [26]) and learning-based methods (DBA-Fusion [30]). For extra reference, we also test the visual-only MAS3R-SLAM [6].

We first focus on the performance of data association. Fig. 8 shows the performance of temporal tracking and cross-temporal matching based on the feed-forward model. For temporal tracking, it can be observed that the feed-forward model provides dense pixel-level associations and is able to directly establish reliable correspondences between frames with large intervals. Compared with traditional multi-frame feature tracking methods, such long-span associations provide more direct and stronger constraints. Besides, moving objects (e.g., cars) can be effectively excluded in the association based on 3D awareness. Regarding cross-temporal matching (for loop closure), the 3D priors embedded in the feed-forward model makes dense matching possible even under extreme viewpoint differences. To be specific, it enables imaginative data associations in cases where the viewpoint difference exceeds 90° , or even when the views are completely opposite—something that is difficult to achieve with conventional feature-based matching methods.

The focus is then put on pose estimation. Considering the relatively large scale, we evaluate the odometry performance using relative pose metrics, following the KITTI [40] odometry benchmark. The results are listed in TABLE I. The corresponding representative trajectory of the data sequence is shown in Fig. 9(a). It can be seen that the proposed MAS3R-Fusion achieves accurate pose estimation, yielding lower relative translation errors compared with both traditional indirect/direct VIO methods and learning-based VIO approaches. This improvement can be attributed to the powerful data association enabled by the feed-forward model, as well as the effective pointmap-alignment-based visual constraints. In addition, the visual-only MAS3R-SLAM almost fails to complete SLAM at such a large scale, whose scale estimation is severely affected by the imperfect information of pointmap regression. The incorporation of inertial information effectively mitigates these errors and fully leverages the strong dense visual constraints for stable metric-scale pose estimation.

Afterwards, we evaluate the global SLAM performance, by activating loop closure and global optimization. For comparison, we test ORB-SLAM3 which supports loop closure and BA-based global optimization. We simply account the absolute translation errors (ATEs) for evaluation [41], which are listed in TABLE II. The corresponding trajectory is shown in Fig. 9(b). It can be observed that the proposed MAS3R-Fusion achieves a significantly lower ATE than ORB-SLAM3. This is

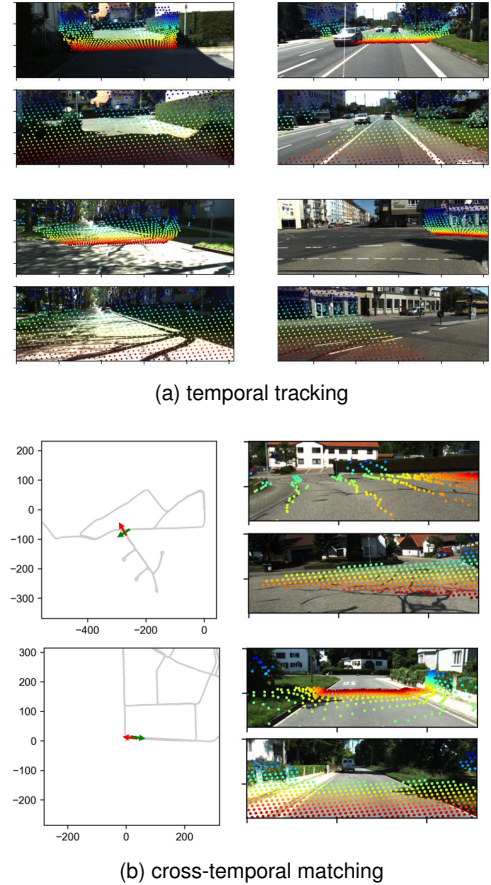


Fig. 8. Pixel-level association for image pairs on KITTI-360 sequences.

partly due to the higher odometry accuracy, and partly because the proposed method incorporates stronger and richer loop closure information. As illustrated in Fig. 8, loop closures under large viewpoint differences allow the system to maintain pose consistency even when driving in opposite directions, which provides favorable conditions for globally consistent mapping.

One of the functionalities of the proposed system is real-time 3D spatial perception with metric scale awareness. In Fig. 10, we qualitatively evaluate this by comparing the proposed system with learning-based dense VIO [30] system and metric depth inference model [42]. From the results, it can be observed that all the three methods are capable of achieving dense perception of the environment with metric scale. Among them, DBA-Fusion primarily relies on BA for reconstructing the environment structure but lacks 3D priors, which leads to scattered points and poor handling of dynamic objects in the scene. The monocular depth model Metric3D v2, through specialized training, demonstrates strong depth estimation performance, particularly in terms of surface normals and edges. However, since it fully depends on inference, objects with ambiguous depth cues can exhibit significant depth/scale errors. In contrast, MAS3R-Fusion preserves the overall 3D structure while leveraging binocular geometry, thereby attaining relatively stable and complete real-time 3D perception performance.

TABLE I
RELATIVE POSE ERRORS OF DIFFERENT VIO SCHEMES ON KITTI-360 DATASET.

Seq.	Desc.	VINS-Fusion		ORB-SLAM3		DM-VIO		MASt3R-SLAM*		DBA-Fusion		MASt3R-Fusion	
		t_{rel}^1	r_{rel}^1	t_{rel}	r_{rel}	t_{rel}	r_{rel}	t_{rel}	r_{rel}	t_{rel}	r_{rel}	t_{rel}	r_{rel}
0000	Suburb	1.897	0.176	2.386	0.117	1.369	0.129	39.64	0.524	0.678	0.105	0.726	0.151
0002	Suburb	1.006	0.199	1.309	0.215	0.724	0.183	43.88	0.600	0.577	0.174	0.504	0.145
0003	Highway	2.754	0.088	7.044	0.151	1.146	0.111	21.59	0.488	1.041	0.114	0.406	0.079
0004	Suburb	1.710	0.193	1.976	0.211	1.063	0.178	48.79	0.887	0.556	0.153	0.770	0.157
0005	Suburb	1.187	0.219	1.414	0.227	0.729	0.224	32.50	0.799	0.619	0.209	0.544	0.208
0006	Suburb	1.349	0.176	1.685	0.184	0.887	0.161	54.09	0.695	0.734	0.166	0.658	0.155
0009	Suburb	1.596	0.144	2.407	0.184	1.379	0.136	54.58	0.570	0.846	0.136	0.631	0.144
0010	Boulevard	3.610	0.216	5.335	0.214	2.130	0.215	47.06	0.513	1.486	0.208	1.138	0.198

* Visual-only, scaled using Sim(3)-based global alignment [41]. ¹ t_{rel} in %, r_{rel} in $^{\circ}/100$ m.

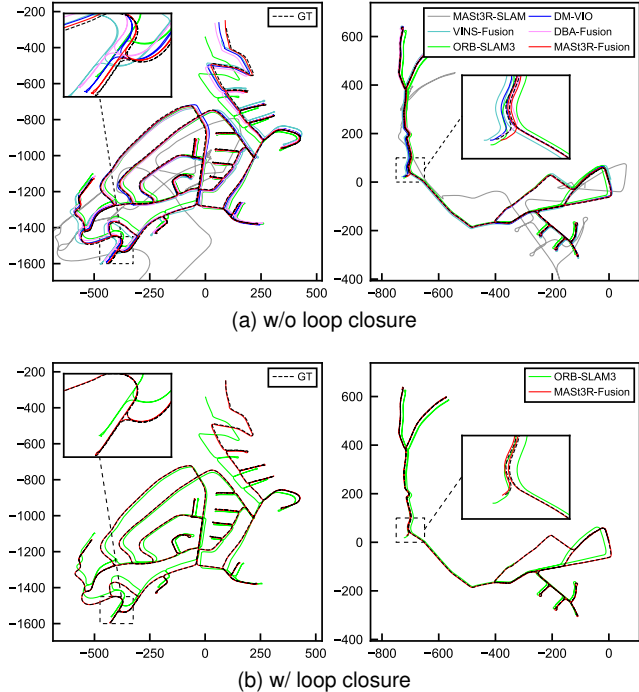


Fig. 9. Estimated trajectories of different V-I SLAM schemes on KITTI-360 sequences.

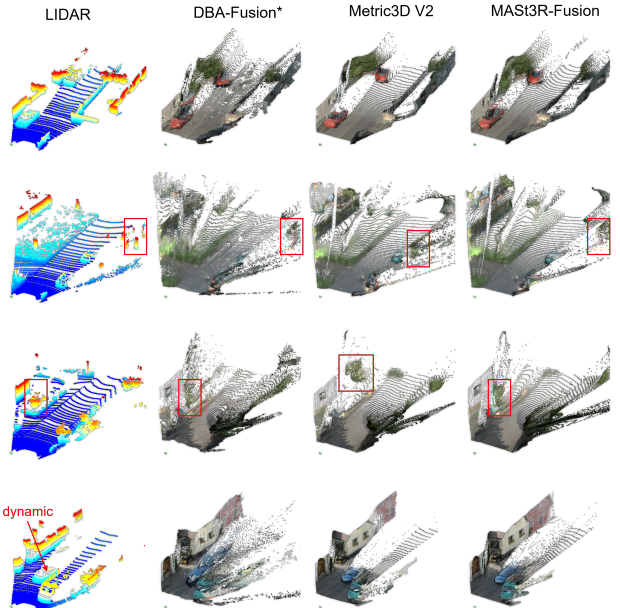


Fig. 10. Real-time 3D perception performance on KITTI-360 sequences. *For DBA-Fusion, which relies on recurrent optical flow, the perception results are obtained with a delay and are therefore not strictly real-time.

TABLE II
ABSOLUTE TRANSLATION ERRORS (M) OF DIFFERENT GLOBAL SLAM SCHEMES (WITH LOOP CLOSURE) ON KITTI-360 DATASET.

Seq.	ORB-SLAM3	MASt3R-Fusion	Leng. (m)
0000	26.03	2.13	8361
0002	32.57	2.82	11195
0003	28.63	0.70	1368
0004	42.82	4.56	8614
0005	10.56	1.28	4561
0006	9.51	2.52	7699
0009	6.95	1.90	8677
0010	45.17	4.38	3340
ave(%)	0.63	0.05	norm.

B. SubT-MRS Dataset

An important issue for general-purpose visual models is their generalization ability. For example, existing monocular depth estimation algorithms can perform well in rooms or driving scenarios, but may face challenges in unseen, unusual

scenes. To evaluate the effectiveness of the algorithm in unconventional scenarios, the V-I dataset from SubT-MRS [39] is employed. This dataset contains three real-world sequences, two collected in karst caves, and one recorded by a quadruped robot transitioning between indoor and outdoor environments.

Similarly, we first focus on the performance of data association. It can be seen from Fig. 11 that in unconventional scenarios (such as caves), the feed-forward model still provides reliable dense feature associations, even when the scene texture is only weakly distinguishable. The matching performance under large viewpoint differences remains excellent, even surpassing the range discernible by the human eye, thereby offering strong potential constraints for global SLAM.

Afterwards, we conducted tests on these data sequences for both real-time and global V-I SLAM. The results of the pose estimation are presented in TABLE III and TABLE IV.

From the real-time SLAM results, it can be observed that MASt3R-Fusion achieves significantly higher pose estimation accuracy than existing methods, providing stable metric-scale

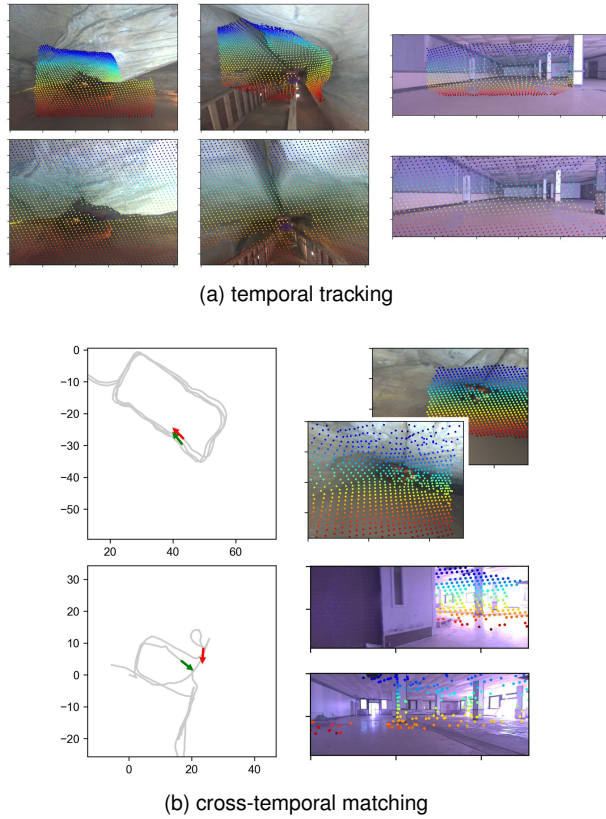


Fig. 11. Pixel-level association for image pairs on SuBT-MRS sequences.

odometry performance. In terms of global SLAM performance, the aggressive loop closure detection delivers impressive results, leading to a substantial reduction in ATEs. This part of the experiments largely validates the generalizability of the feed-forward model approach on open scenarios when combined with IMU information.

TABLE III

ABSOLUTE TRANSLATION ERRORS (M) OF DIFFERENT VIO SCHEMES ON SUBT-MRS DATASET.

Seq.	VINS	ORB	DM-VIO	DBA	M-Fus.	Leng. (m)
handheld1	5.64	2.16	14.54	1.78	1.07	394
handheld2	2.32	2.42	4.94	2.09	1.13	509
overexposure	2.61	1.27	2.97	1.85	0.99	509
ave(%)	0.80	0.42	1.74	0.41	0.23	norm.

TABLE IV

ABSOLUTE TRANSLATION ERRORS (M) OF DIFFERENT GLOBAL SLAM SCHEMES (WITH LOOP CLOSURE) ON SUBT-MRS DATASET.

Seq.	ORB-SLAM3	MAS3R-Fusion	Leng. (m)
handheld1	1.48	0.26	394
handheld2	2.14	1.04	395
overexposure	1.07	0.43	509
ave(%)	0.37	0.13	norm.

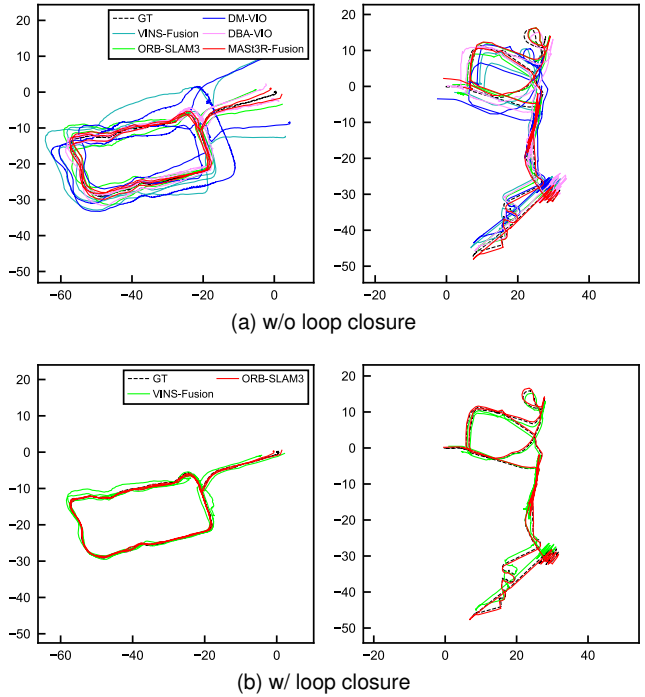


Fig. 12. Estimated trajectories of different V-I SLAM schemes on SuBT-MRS sequences.

C. Wuhan Urban Dataset

In addition to the evaluation of the V-I system, to further evaluate the algorithm's performance in real-world road scenarios (with dynamic objects) and to consider its integration with global GNSS measurements, we turn to the self-collected multi-sensor dataset acquired in Wuhan City. The dataset contains two sequences, with their trajectories shown in Fig. 13. We take the classical VINS-Fusion as the baseline, whichs supports both real-time pose estimation and global fusion with GNSS.

First, we tested several different pose estimation schemes based on V-I data, including real-time VIO and global SLAM. The corresponding trajectory is shown in Fig. 14. It can be observed that in large-scale road environments (with long straight segments), the traditional VIO algorithm suffers from significant scale estimation errors due to weak observability [43]. In contrast, the proposed MAS3R-Fusion method, by combining probabilistic marginalization with Sim(3)-based visual constraints, can effectively control and correct scale drift. Besides, after introducing loop closure constraints, the position error caused by attitude drift is greatly reduced, and the trajectory accuracy is further improved.

Second, the global positioning performance with GNSS integration is focused on. The positioning errors are depicted in Fig. 15. From the results, it can be observed that GNSS RTK exhibits many gross errors and periods of unavailability, especially in sequence (a). For VINS-Fusion, in which GNSS positions are fused with VIO-provided relative poses loosely through a pose graph, the position estimation errors during GNSS-degraded periods cannot be effectively suppressed, since the position residuals cannot be probabilistically distributed across all poses. This further undermines the de-

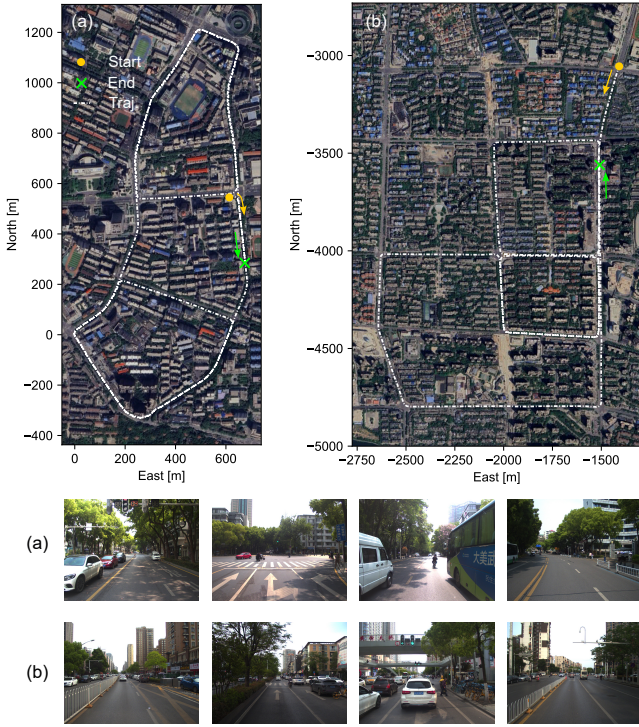


Fig. 13. Trajectories and environmental images of sequences in the self-collected Wuhan urban dataset.

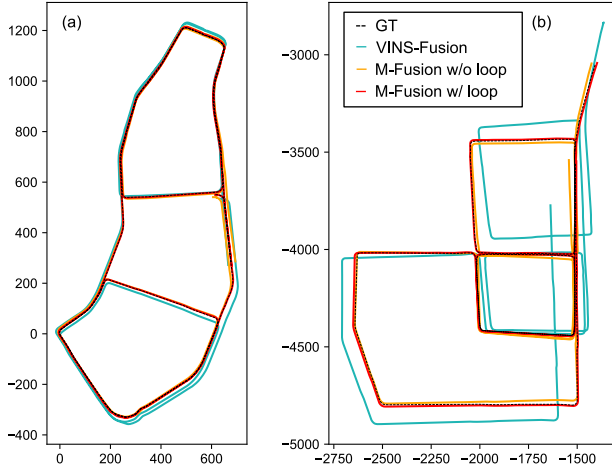


Fig. 14. Estimated trajectories of different V-I SLAM schemes on Wuhan urban sequences.

tection and mitigation of GNSS gross errors. In contrast, in the proposed MAST3R-Fusion, the complete and precise V-I information is fully preserved into the factor graph, effectively resisting GNSS gross errors through iterative optimization and maintaining decimeter-level accuracy.

Moreover, to enrich the variability of GNSS observation conditions in the tests, we use simulated GNSS data based on ground truth with intermittent outages to assess the robustness of the algorithm. The results are shown in Fig. 16, which further demonstrate the effectiveness of the proposed method in recovering globally optimal trajectories. Impressively, with 100-second GNSS outages, the global factor graph can still achieve mostly sub-meter level trajectory smoothing, and the

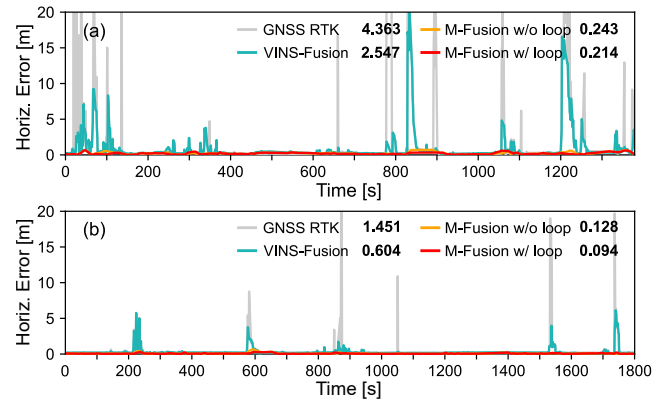


Fig. 15. Horizontal errors of different absolute positioning schemes with GNSS RTK integration. The bolded numbers indicate the root mean square errors (RMSEs).

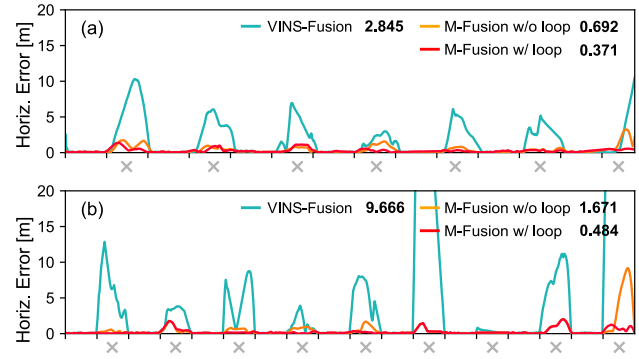


Fig. 16. Horizontal errors of different absolute positioning schemes with simulated GNSS integration. The gray crosses indicate simulated GNSS outages (100-second). The bolded numbers indicate the RMSEs.

introduction of cross-temporal associations further reduces the overall error.

D. Reconstruction Results

Finally, we qualitatively evaluate the dense 3D perception and scene reconstruction performance of the proposed method under different scenarios. As shown in Fig. 17, the proposed method can effectively recover the dense structure of the scene with metric scale. For revisited trajectories, the consistency of scene reconstruction can be achieved, which based on the high-accuracy pose estimation and effective cross-temporal data association.

VIII. CONCLUSION

In this work, we presented *Mast3r-Fusion*, a novel multi-sensor-assisted visual SLAM framework that tightly integrates feed-forward pointmap regression with complementary sensor information, including inertial and GNSS measurements. By introducing Sim(3)-based visual alignment constraints into a universal metric-scale SE(3) factor graph, our system achieves accurate pose tracking, metric-scale 3D structure perception and globally consistent SLAM. Experimental results on both public benchmarks and self-collected datasets indicate the substantial improvements over existing visual and multi-sensor

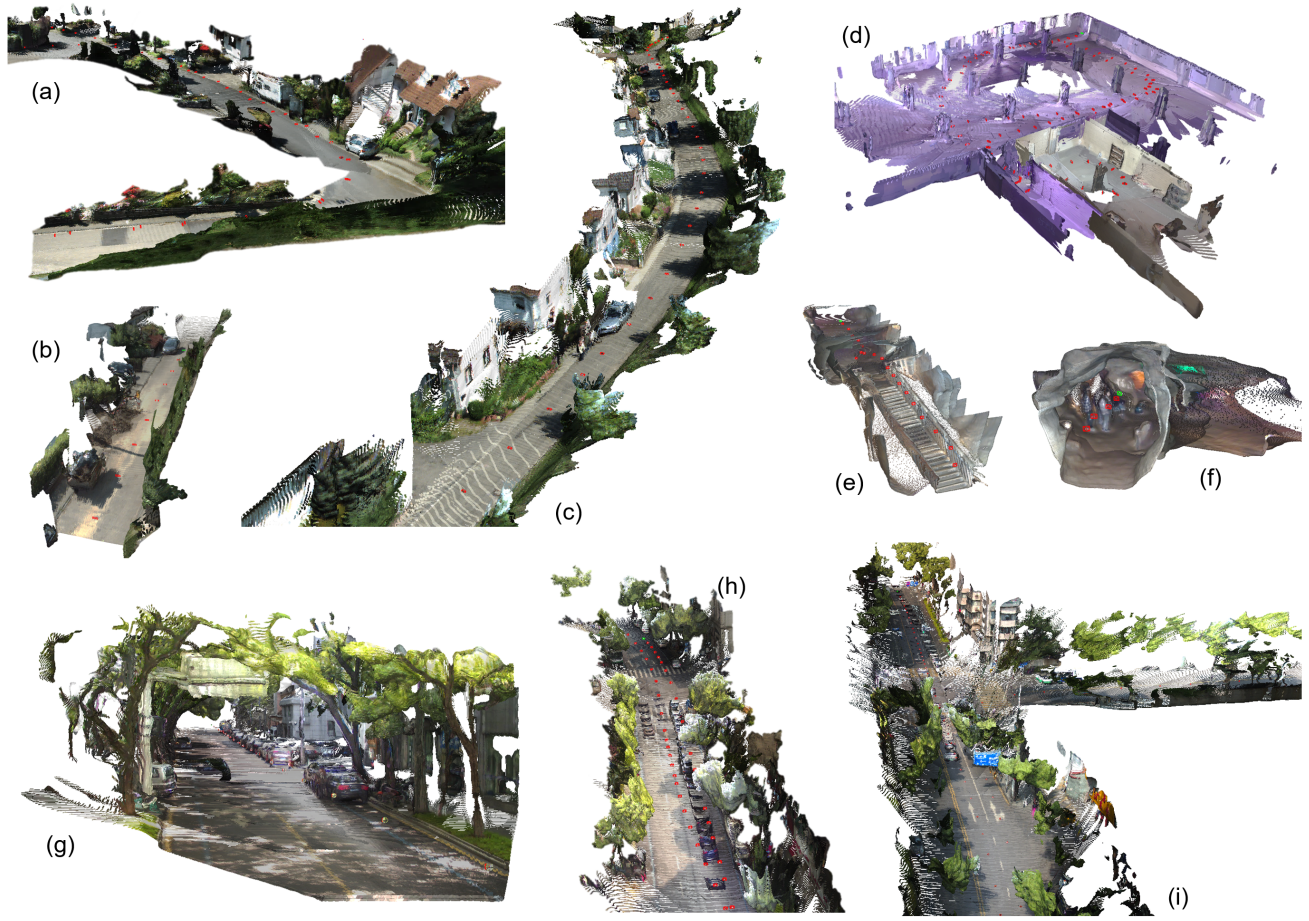


Fig. 17. Reconstruction results. (a-c) KITTI-360. (d-f) SuBT-MRS. (g-i) Self-collected Wuhan urban dataset.

SLAM systems, showing high functionality in terms of localization and mapping.

This work facilitates robust and accurate pose estimation and mapping in ubiquitous scenarios. In the future, our research will focus on semantic fusion and advanced scene representations to support embodied navigation tasks.

ACKNOWLEDGMENTS

The implemented MAS3R-Fusion is developed by the GREAT Group, School of Geodesy and Geomatics, Wuhan University. The numerical calculations in this paper have been done on the supercomputing system at the Supercomputing Center of Wuhan University.

REFERENCES

- [1] I. A. Kazerouni, L. Fitzgerald, G. Dooly, and D. Toal, “A survey of state-of-the-art on visual SLAM,” *Expert Systems with Applications*, vol. 205, p. 117734, 2022. [Online]. Available: <https://www.sciencedirect.com/science/article/pii/S0957417422010156>
- [2] S. Mokssit, D. B. Licea, B. Guermah, and M. Ghogho, “Deep learning techniques for visual slam: A survey,” *IEEE Access*, vol. 11, pp. 20 026–20 050, 2023, publisher: IEEE.
- [3] S. Wang, V. Leroy, Y. Cabon, B. Chidlovskii, and J. Revaud, “DUS3R: Geometric 3D Vision Made Easy,” in *Proceedings of the IEEE/CVF Conference on Computer Vision and Pattern Recognition (CVPR)*. IEEE, Jun. 2024, pp. 20 697–20 709. [Online]. Available: https://openaccess.thecvf.com/content/CVPR2024/html/Wang_DUS3R_Geometric_3D_Vision_Made_Easy_CVPR_2024_paper.html
- [4] V. Leroy, Y. Cabon, and J. Revaud, “Grounding Image Matching in 3D with MAS3R,” *arXiv preprint arXiv:2406.09756*, 2024. [Online]. Available: <https://arxiv.org/abs/2406.09756>
- [5] J. Wang, M. Chen, N. Karaev, A. Vedaldi, C. Rupprecht, and D. Novotny, “VG3T: Visual Geometry Grounded Transformer,” in *Proceedings of the IEEE/CVF Conference on Computer Vision and Pattern Recognition (CVPR)*. IEEE, 2025, pp. 1621–1630. [Online]. Available: https://openaccess.thecvf.com/content/CVPR2025/papers/Wang_VG3T_Visual_Geometry_Grounded_Transformer_CVPR_2025_paper.pdf
- [6] R. Murai, E. Dexheimer, and A. J. Davison, “MAS3R-SLAM: Real-Time Dense SLAM with 3D Reconstruction Priors,” in *Proceedings of the IEEE/CVF Conference on Computer Vision and Pattern Recognition (CVPR)*. IEEE, Jun. 2025, pp. 16 695–16 705. [Online]. Available: https://openaccess.thecvf.com/content/CVPR2025/html/Murai_MAS3R-SLAM_Real-Time_Dense_SLAM_with_3D_Reconstruction_Priors_CVPR_2025_paper.html
- [7] D. Maggio, H. Lim, and L. Carlone, “VG3T-SLAM: Dense RGB SLAM Optimized on the SL(4) Manifold,” *arXiv preprint arXiv:2505.12549*, 2025. [Online]. Available: <https://arxiv.org/abs/2505.12549>
- [8] H. Wang and L. Agapito, “3D Reconstruction with Spatial Memory,” *arxiv*, vol. 2408.16061, pp. 1–14, Aug. 2024, arXiv:2408.16061 [cs]. [Online]. Available: <http://arxiv.org/abs/2408.16061>
- [9] J. Zhang, C. Herrmann, J. Hur, V. Jampani, T. Darrell, F. Cole, D. Sun, and M.-H. Yang, “MonST3R: A Simple Approach for Estimating

- Geometry in the Presence of Motion,” *arXiv preprint arxiv:2410.03825*, 2024. [Online]. Available: <https://arxiv.org/abs/2410.03825>
- [10] Y. Wang, J. Zhou, H. Zhu, W. Chang, Y. Zhou, Z. Li, J. Chen, J. Pang, C. Shen, and T. He, “Pi³: Scalable Permutation-Equivariant Visual Geometry Learning,” *arXiv preprint arxiv:2507.13347*, 2025. [Online]. Available: <https://arxiv.org/abs/2507.13347>
- [11] W. Jang, P. Weinzaepfel, V. Leroy, L. Agapito, and J. Revaud, “Pow3R: Empowering Unconstrained 3D Reconstruction with Camera and Scene Priors,” *2025 IEEE/CVF Conference on Computer Vision and Pattern Recognition (CVPR)*, pp. 1071–1081, 2025. [Online]. Available: <https://api.semanticscholar.org/CorpusID:277244721>
- [12] C. Campos, R. Elvira, J. J. G. Rodríguez, J. M. M. Montiel, and J. D. Tardós, “ORB-SLAM3: An Accurate Open-Source Library for Visual, Visual-Inertial and Multi-Map SLAM,” *IEEE Transactions on Robotics*, vol. 37, no. 6, pp. 1874–1890, 2021. [Online]. Available: <https://ieeexplore.ieee.org/document/9406553>
- [13] D. DeTone, T. Malisiewicz, and A. Rabinovich, “Superpoint: Self-supervised interest point detection and description,” in *Proceedings of the IEEE conference on computer vision and pattern recognition workshops*, 2018, pp. 224–236. [Online]. Available: https://openaccess.thecvf.com/content_cvpr_2018_workshops/w9/html/DeTone_SuperPoint_Self-Supervised_Interest_CVPR_2018_paper.html
- [14] D. Li, X. Shi, Q. Long, S. Liu, W. Yang, F. Wang, Q. Wei, and F. Qiao, “DXSLAM: A robust and efficient visual SLAM system with deep features,” in *2020 IEEE/RSJ International conference on intelligent robots and systems (IROS)*. IEEE, 2020, pp. 4958–4965. [Online]. Available: <https://ieeexplore.ieee.org/abstract/document/9340907/>
- [15] K. Tateno, F. Tombari, I. Laina, and N. Navab, “Cnn-slam: Real-time dense monocular slam with learned depth prediction,” in *Proceedings of the IEEE conference on computer vision and pattern recognition*, 2017, pp. 6243–6252. [Online]. Available: http://openaccess.thecvf.com/content_cvpr_2017/html/Tateno_CNN-SLAM_Real-Time_Dense_CVPR_2017_paper.html
- [16] X. Wang, Y. Zhuang, X. Cao, J. Huai, Z. Zhang, Z. Zheng, and N. El-Sheimy, “GAT-LSTM: A feature point management network with graph attention for feature-based visual SLAM in dynamic environments,” *ISPRS Journal of Photogrammetry and Remote Sensing*, vol. 224, pp. 75–93, 2025. [Online]. Available: <https://www.sciencedirect.com/science/article/pii/S0924271625001091>
- [17] A. Adkins, T. Chen, and J. Biswas, “ObVi-SLAM: Long-Term Object-Visual SLAM,” *IEEE Robotics and Automation Letters*, vol. 9, no. 3, pp. 2909–2916, Mar. 2024, conference Name: IEEE Robotics and Automation Letters. [Online]. Available: <https://ieeexplore.ieee.org/abstract/document/10423794>
- [18] S. Yang and S. Scherer, “Cubeslam: Monocular 3-d object slam,” *IEEE Transactions on Robotics*, vol. 35, no. 4, pp. 925–938, 2019, publisher: IEEE. [Online]. Available: <https://ieeexplore.ieee.org/abstract/document/8708251/>
- [19] H. Zhou, Z. Guo, S. Liu, L. Zhang, Q. Wang, Y. Ren, and M. Li, “MoD-SLAM: Monocular Dense Mapping for Unbounded 3D Scene Reconstruction,” *arXiv preprint arxiv:2402.03762*, 2024. [Online]. Available: <https://arxiv.org/abs/2402.03762>
- [20] H. Matsuki, R. Murai, P. H. J. Kelly, and A. J. Davison, “Gaussian Splatting SLAM,” in *Proceedings of the IEEE/CVF Conference on Computer Vision and Pattern Recognition (CVPR)*, 2024, pp. 1234–1243. [Online]. Available: <https://arxiv.org/abs/2404.01423>
- [21] Z. Teed and J. Deng, “Droid-slam: Deep visual slam for monocular, stereo, and rgb-d cameras,” *Advances in neural information processing systems*, vol. 34, pp. 16558–16569, 2021. [Online]. Available: <https://proceedings.neurips.cc/paper/2021/hash/89fcd07f02b6785b92134bd6c1d0fa42-Abstract.html>
- [22] Y. Liu, S. Dong, S. Wang, Y. Yin, Y. Yang, Q. Fan, and B. Chen, “SLAM3R: Real-Time Dense Scene Reconstruction from Monocular RGB Videos,” *arXiv preprint arxiv:2412.09401*, 2024. [Online]. Available: <https://arxiv.org/abs/2412.09401>
- [23] S. Leutenegger, S. Lynen, M. Bosse, R. Siegwart, and P. T. Furgale, “Keyframe-Based Visual-Inertial SLAM Using Nonlinear Optimization,” *The International Journal of Robotics Research*, vol. 34, no. 3, pp. 314–334, 2015. [Online]. Available: <https://doi.org/10.1177/0278364914565495>
- [24] T. Qin, P. Li, and S. Shen, “Vins-mono: A robust and versatile monocular visual-inertial state estimator,” *IEEE transactions on robotics*, vol. 34, no. 4, pp. 1004–1020, 2018, publisher: IEEE. [Online]. Available: <https://ieeexplore.ieee.org/abstract/document/8421746>
- [25] L. Von Stumberg, V. Usenko, and D. Cremers, “Direct sparse visual-inertial odometry using dynamic marginalization,” in *2018 IEEE International Conference on Robotics and Automation (ICRA)*. IEEE, 2018, pp. 2510–2517.
- [26] L. v. Stumberg and D. Cremers, “DM-VIO: Delayed Marginalization Visual-Inertial Odometry,” *IEEE Robotics and Automation Letters (RAL) & International Conference on Robotics and Automation (ICRA)*, vol. 7, no. 2, pp. 1408–1415, 2022.
- [27] L. Wang, H. Tang, T. Zhang, Y. Wang, Q. Zhang, and X. Niu, “PO-KF: A Pose-Only Representation-Based Kalman Filter for Visual Inertial Odometry,” *IEEE Internet of Things Journal*, vol. 12, no. 10, pp. 14 856–14 875, 2025.
- [28] Z. Xiao and S. Li, “A real-time, robust and versatile visual-SLAM framework based on deep learning networks,” 2024, *eprint: 2405.03413*. [Online]. Available: <https://arxiv.org/abs/2405.03413>
- [29] H. Luo, Y. Liu, C. Guo, Z. Li, and W. Song, “SuperVINS: A Real-Time Visual-Inertial SLAM Framework for Challenging Imaging Conditions,” *arXiv*, vol. 2407.21348, pp. 1–16, Nov. 2024, arXiv:2407.21348 [cs]. [Online]. Available: <http://arxiv.org/abs/2407.21348>
- [30] Y. Zhou, X. Li, S. Li, X. Wang, S. Feng, and Y. Tan, “DBA-Fusion: Tightly Integrating Deep Dense Visual Bundle Adjustment With Multiple Sensors for Large-Scale Localization and Mapping,” *IEEE Robotics and Automation Letters*, vol. 9, no. 7, pp. 6138–6145, 2024.
- [31] X. Peng, Z. Liu, W. Li, P. Tan, S. Y. Cho, and Q. Wang, “Dvi-slam: A dual visual inertial slam network,” in *2024 IEEE International Conference on Robotics and Automation (ICRA)*. IEEE, 2024, pp. 12 020–12 026. [Online]. Available: <https://ieeexplore.ieee.org/abstract/document/10610042/>
- [32] L. Han, Y. Lin, G. Du, and S. Lian, “Deepvio: Self-supervised deep learning of monocular visual inertial odometry using 3d geometric constraints,” in *2019 IEEE/RSJ International Conference on Intelligent Robots and Systems (IROS)*. IEEE, 2019, pp. 6906–6913. [Online]. Available: <https://ieeexplore.ieee.org/abstract/document/8968467/>
- [33] X. Li, S. Li, Y. Zhou, Z. Shen, X. Wang, X. Li, and W. Wen, “Continuous and precise positioning in urban environments by tightly coupled integration of GNSS, INS and vision,” *IEEE Robotics and Automation Letters*, vol. 7, no. 4, pp. 11 458–11 465, 2022, publisher: IEEE. [Online]. Available: <https://ieeexplore.ieee.org/abstract/document/9866851/>
- [34] T. Qin, S. Cao, J. Pan, P. Li, and S. Shen, “VINS-Fusion: An Optimization-Based Multi-Sensor State Estimator,” 2020. [Online]. Available: <https://github.com/HKUST-Aerial-Robotics/VINS-Fusion>
- [35] S. Cao, X. Lu, and S. Shen, “GVINS: Tightly Coupled GNSS–Visual–Inertial Fusion for Smooth and Consistent State Estimation,” *IEEE Transactions on Robotics*, vol. 38, no. 4, pp. 2004–2021, 2021. [Online]. Available: <https://arxiv.org/abs/2103.07899>
- [36] B. Triggs, P. F. McLauchlan, R. I. Hartley, and A. W. Fitzgibbon, “Bundle adjustment—a modern synthesis,” in *International workshop on vision algorithms*. Springer, 1999, pp. 298–372.
- [37] C. Forster, L. Carlone, F. Dellaert, and D. Scaramuzza, “IMU preintegration on manifold for efficient visual-inertial maximum-a-posteriori estimation,” 2015, publisher: Georgia Institute of Technology. [Online]. Available: <https://repository.gatech.edu/handle/1853/55417>
- [38] Y. Liao, J. Xie, and A. Geiger, “KITTI-360: A novel dataset and benchmarks for urban scene understanding in 2d and 3d,” *IEEE Transactions on Pattern Analysis and Machine Intelligence*, vol. 45, no. 3, pp. 3292–3310, 2022, publisher: IEEE. [Online]. Available: <https://ieeexplore.ieee.org/abstract/document/9786676/>
- [39] S. Zhao, Y. Gao, T. Wu, D. Singh, R. Jiang, H. Sun, M. Sarawata, Y. Qiu, W. Whittaker, I. Higgins, Y. Du, S. Su, C. Xu, J. Keller, J. Karhade, L. Nogueira, S. Saha, J. Zhang, W. Wang, C. Wang, and S. Scherer, “SubT-MRS Dataset: Pushing SLAM Towards All-weather Environments,” in *Proceedings of the IEEE/CVF Conference on Computer Vision and Pattern Recognition (CVPR)*, Jun. 2024, pp. 22 647–22 657.
- [40] A. Geiger, P. Lenz, and R. Urtasun, “Are we ready for autonomous driving? The KITTI vision benchmark suite,” in *2012 IEEE Conference on Computer Vision and Pattern Recognition*, Jun. 2012, pp. 3354–3361, iSSN: 1063-6919. [Online]. Available: <https://ieeexplore.ieee.org/abstract/document/6248074>
- [41] M. Grupp, “evo: Python package for the evaluation of odometry and SLAM.” 2017. [Online]. Available: <https://github.com/MichaelGrupp/evo>
- [42] M. Hu, W. Yin, C. Zhang, Z. Cai, X. Long, H. Chen, K. Wang, G. Yu, C. Shen, and S. Shen, “Metric3D v2: A Versatile Monocular Geometric Foundation Model for Zero-Shot Metric Depth and Surface Normal Estimation,” *IEEE Transactions on Pattern Analysis and Machine Intelligence*, vol. 46, no. 12, pp. 10 579–10 596, 2024.

- [43] A. Martinelli, "Visual-inertial structure from motion: Observability and resolvability," in *2013 IEEE/RSJ International Conference on Intelligent Robots and Systems*, Nov. 2013, pp. 4235–4242, iSSN: 2153-0866. [Online]. Available: <https://ieeexplore.ieee.org/abstract/document/6696963>